01 Apr 2018

Direct Metal Laser-sintered Stainless Steel: Comparison Of Microstructure And Hardness Between Different Planes

M. Ghasri-Khouzani

H. Peng

R. Attardo

P. Ostiguy

et. al. For a complete list of authors, see https://scholarsmine.mst.edu/mec_aereng_facwork/5187

Recommended Citation

M. Ghasri-Khouzani et al., "Direct Metal Laser-sintered Stainless Steel: Comparison Of Microstructure And Hardness Between Different Planes," *International Journal of Advanced Manufacturing Technology*, vol. 95, no. 9 thru 12, pp. 4031 - 4037, Springer, Apr 2018.
The definitive version is available at https://doi.org/10.1007/s00170-017-1528-y

The International Journal of Advanced Manufacturing Technology (2018) 95:4031–4037
https://doi.org/10.1007/s00170-017-1528-y

ORIGINAL ARTICLE

Direct metal laser-sintered stainless steel: comparison of microstructure and hardness between different planes

M. Ghasri-Khouzani[1] · H. Peng[2] · R. Attardo[3] · P. Ostiguy[3] · J. Neidig[4] · R. Billo[5] · D. Hoelzle[6] · M. R. Shankar[1]

Received: 13 October 2017 / Accepted: 18 December 2017 / Published online: 3 January 2018

Abstract
Microstructural analysis and micro-hardness measurements were performed on different planes of 316L stainless steel fabricated by direct metal laser sintering (DMLS) technique. A fine cellular network was observed within the steel microstructure, where morphology of most cells changed from columnar on XZ-plane (vertical section) to equiaxed on XY-plane (horizontal section). Correspondingly, morphology of most grains was found to alter from columnar for the XZ-plane to equiaxed in the case of the XY-plane. Moreover, X-ray diffraction (XRD) analysis revealed a fully austenitic structure for both the planes. The average micro-hardness value for the XZ-plane and XY-plane was insignificantly (≈ 3%) different, which was attributed to the random grain orientation observed on both the planes. However, the average micro-hardness of the DMLS-fabricated 316L stainless steel in this contribution was approximately 25% higher than that of the as-cast one.

Keywords Additive manufacturing · Stainless steel · Microstructure · Hardness · DMLS

1 Introduction

Additive manufacturing (AM) has received significant attention over the last two decades mainly due to its capabilities to produce near-net-shape parts of complex geometry [1, 2]. In contrast to conventional machining in which excessive materials are removed from the work piece, during AM processes, the desire component is created in a layer-by-layer manner. Thus, AM technology is considered as a new revolution in manufacturing industry [3, 4]. However, AM processes are mostly appreciated for small fabrication runs with expensive materials due to their relatively low production rates. Direct metal laser sintering (DMLS) is a common metal-based AM technique, in which a high-power laser beam is used to selectively fuse metal powders to fabricate functional dense components. This technique has been used for various metallic materials such as aluminum alloys [5, 6], nickel-based superalloys [7, 8], titanium alloys [9], and steels [10–12]. During DMLS, each powder layer undergoes repeated heating-cooling cycles which lead to microstructures different from ones obtained through conventional manufacturing processes [13].

AISI 316L stainless steel is a low-carbon, high-molybdenum stainless steel which has widespread application in marine, medical, nuclear, and oil industries due to its high strength and corrosion resistance. Additively manufactured 316L stainless steel parts have exhibited better mechanical properties compared to their cast and forged counterparts [14–16]. Several studies have investigated the microstructure and mechanical behavior of 316L stainless steel fabricated by AM [14, 17–22]. For example, Zhang et al. [21] found a cellular microstructure and anisotropic mechanical properties for 316L stainless steel made by laser metal deposition shaping. In another study, Zietala et al. [22] used the laser-engineered nest shaping (LENS) technique to fabricate 316L stainless steel. Their characterization revealed BCC ferrite in

✉ M. Ghasri-Khouzani
mog20@pitt.edu

[1] Department of Industrial Engineering, University of Pittsburgh, Pittsburgh, PA 15261, USA

[2] Department of Aerospace and Mechanical Engineering, University of Notre Dame, Notre Dame, IN 46556, USA

[3] DePuy Synthes, Johnson & Johnson Company, Raynham, MA 02767, USA

[4] ITAMCO, Plymouth, IN 46563, USA

[5] Department of Computer Science and Engineering, University of Notre Dame, Notre Dame, IN 46556, USA

[6] Department of Mechanical and Aerospace Engineering, The Ohio State University, Columbus, OH 43210, USA

the microstructure which enhanced the mechanical properties. Saeidi et al. [19], achieved crack-free 316L stainless steel with fully austenitic microstructure using the laser melting technique. The focus of these studies has been the evaluation of microstructure and mechanical properties of the bulk AM sample without making distinction between different part planes (i.e., XY-plane, XZ-plane). Since the material performance required for various planes of an AM part in service can be different, it is necessary to compare the microstructure and mechanical properties of different planes. Thus, the objective of the present contribution is to distinguish the difference in microstructure and mechanical properties of different AM part planes. Disk-shaped 316L stainless steel was fabricated using DMLS technique and sectioned both parallel and perpendicular to the build direction. The resulting microstructure and mechanical properties of the sections are discussed thoroughly.

2 Experimental procedure

2.1 Feedstock powder and DMLS technique

The starting feedstock material was a gas atomized 316L stainless steel powder, whose chemical composition is listed in Table 1. Disk-shaped samples with 45 mm diameter and 20 mm height were fabricated by DMLS method using an EOS M290 machine, equipped with an Yb-fiber laser. The optimized process parameters for the 316L stainless steel suggested by Electro-Optical Systems (EOS) company were employed including 20 μm powder layer thickness, 195 W laser power, 1083 mm/s scan speed, and 80 μm hatch spacing. All the samples were built using an alternating scan pattern, where the hatching direction of each layer was rotated by 67° form that of the previous one, as schematically depicted in Fig. 1. To maintain the oxygen level in the build chamber less than 0.1%, an ultra-high purity argon gas was purged into it during the fabrication process. The build plate temperature was kept at 80 °C to reduce stresses imposed by thermal cycles. The build plate was a hot-rolled mild steel panel with dimensions of 252 mm × 252 mm × 18 mm. All samples were printed on top of Materialise Magics block style support structures, which were used to reduce distortion caused by thermal stresses and also facilitate sample detachment from the build plate. The location of the support structure with respect to an individual sample, and base plate as well as the support structure parameters is schematically illustrated in Fig. 2. For all samples, the same support structure parameters were employed as listed in Table 2. An image of the printed samples is presented in Fig. 3.

Table 1 Chemical composition of 316L stainless steel powder used as the feedstock material (wt.%)

C	Cr	Mn	Mo	N	Ni	O	S	Si	Fe
0.03	17.9	2.0	2.4	0.1	13.9	0.04	0.01	0.75	Balance

2.2 Microstructural characterization

For microstructural characterization, the as-built samples were cross-sectioned both parallel and perpendicular to the build direction, followed by grinding and polishing down to a 0.05 μm finish. For optical and scanning electron microscopy (SEM), samples were etched by aqua regia for 20 s. The microstructure of the components was examined using a Keyence VHX-600 optical microscope and FEI Apreo SEM at an operating voltage of 15 kV and a working distance of 10 mm. The grain structure and crystallographic orientation distribution of the as-built components were studied using electron back-scattered diffraction (EBSD) via a FEI Apreo SEM with an accelerating voltage of 20 kV and working distance of 16 mm. The step size was 0.6 μm on all scans to obtain sufficient resolution. TexSEM Laboratory (TSL) software was used for the operation and control of all EBSD analyses as well as analysis of the EBSD results. X-ray diffraction (XRD) analysis was conducted using a Bruker D8 Discover diffractometer equipped with a Cu Kα radiation ($\lambda = 1.5407$ Å). Spectra were taken in the range of 2θ from 30° to 100° with a 0.02° step size.

2.3 Micro-hardness measurements

Vickers micro-hardness measurements on both vertical and horizontal sections of samples were performed with LECO LM800 using a test force of 0.98 N and dwell time of 10 s. The sections were ground and polished but not etched before the micro-hardness tests. In order to investigate possible influence of location (within the same plane) on hardness, indentations were carried out along z direction on XZ-plane and x direction on XY-plane. The distance between indentations was 0.5 mm.

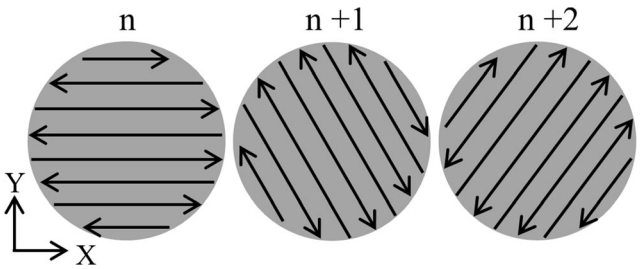

Fig. 1 Schematic illustration of scan pattern for three consecutive powder layers

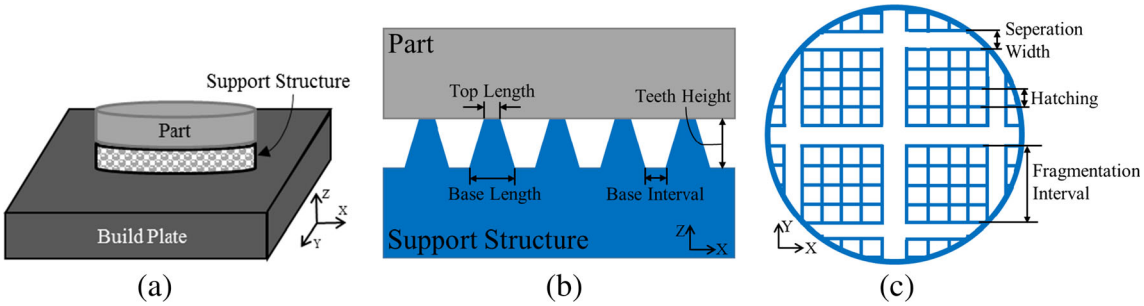

Fig. 2 **a** Schematic of support structure location with respect to an individual sample and base plate. **b**, **c** Schematic of support structure parameters

3 Results and discussion

3.1 Microstructural observations

Optical microscopy was used to analyze the geometrical parameters of the melt pools. Typical optical micrographs of the as-built disk, sectioned parallel to both front surface (XZ-plane) and top surface (XY-plane), are illustrated in Fig. 4. The melt pools were approximately half-cylindrical in shape with an arc-shaped cross-section, as depicted in Fig. 4a. The half-cylindrical geometry is attributed to the Gaussian energy density distribution of the laser beam [23], where the beam center has the greatest energy density. The melt pool depth was measured from Fig. 4a using pixel count to be 86 ± 9 μm. Given the employed powder layer thickness of 20 μm, it can be found that significant remelting occurred across the layers during the part fabrication. From Fig. 4b, it is evident that the scan vectors were not unidirectional. The angle between the vectors was measured to be 67°, which is the same as the angle by which the scan direction rotated between the successive powder layers (see Fig. 1). Since the sample was not ground and polished perfectly perpendicular to the build direction, multiple layers are present in the micrograph as shown in Fig. 4b. From this micrograph, the melt pool width was measured to be 195 ± 18 μm, which was significantly larger than the applied hatch spacing (80 μm) revealing the overlap of the melt pools between the adjacent scan tracks. This is in agreement with previous observations of the 316L stainless steel fabricated by SLM [20, 24].

Table 2 Support structure parameters (mm)

Total height	Fragmentation	Hatching	Teeth height	Teeth base interval	Teeth base length	Teeth top length
5	X-interval = 4 Y-interval = 4 separation width = 0.2	X = 0.8 Y = 0.8	0.5	0	0.5	0.2

SEM was carried out to examine the microstructural features of the DMLS-fabricated samples in more detail. Figure 5 illustrates SEM micrographs obtained from both the vertical section (XZ-plane) and horizontal section (XY-plane) of the as-built 316L stainless steel. The microstructures comprised a cellular network, where the cell boundaries were enriched in molybdenum (Mo) [19, 25]. During the DMLS, austenite solidified first as the cells which were kinetically favored, when the solidifying front rejected Mo into the melt and the remaining Mo then solidified between the cells. Since Mo solubility in austenite increased due to the very fast solidification, the amount of segregating Mo was relatively small leading to thin cellular boundary formation. This solidification structure is common in the additively manufactured 316L stainless steel components [19, 25], but it is significantly different from that of cast ones [26]. From Fig. 5, it can also be seen that the cells within the same melt pool exhibited different morphologies (columnar or equiaxed), where the area fraction of the columnar cells in the XZ-plane (Fig. 5a) was significantly larger than that in the XY-plane (Fig. 5b). Moreover, the XY-plane contained a higher area fraction of the Mo-enriched cell boundaries compared to the XZ-plane. Since the presence of the Mo-enriched cell boundaries in the microstructure

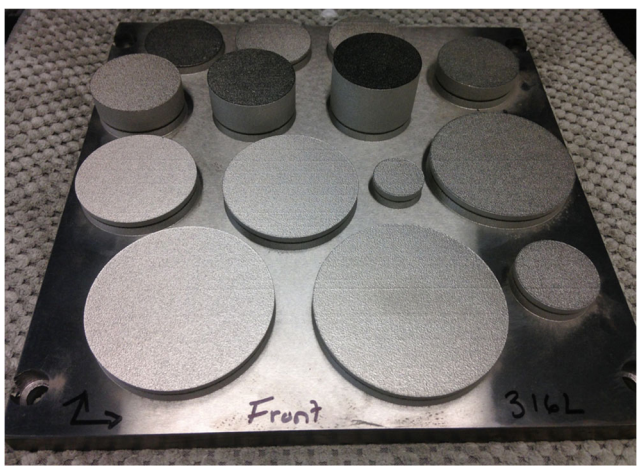

Fig. 3 Image of the DMLS-fabricated samples

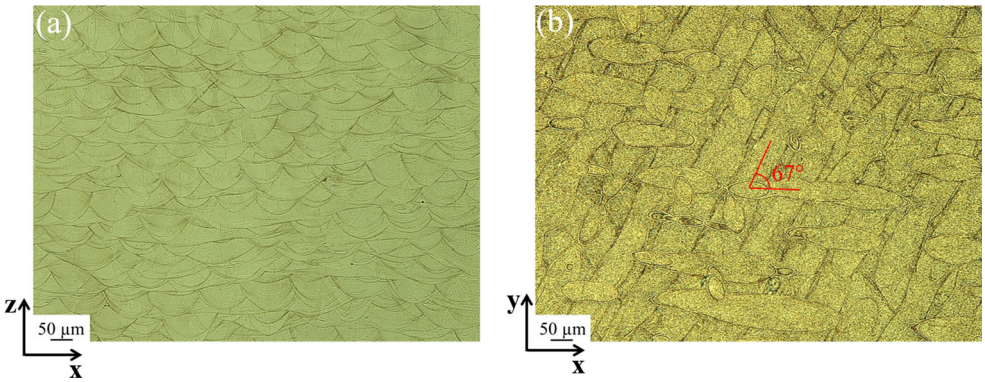

Fig. 4 Optical light microscopy images of the as-built 316L stainless steel disk. **a** Vertical section (front surface). **b** Horizontal section (top surface)

degrades the corrosion resistance of the AM 316L stainless steel [25], the XZ-plane is expected to exhibit a higher corrosion resistance than the XY-plane. Thus, comparison of the corrosion resistance between the two planes should be the subject of future study.

XRD technique was used to analyze the constituent phases of the as-fabricated 316L stainless steel. Figure 6 depicts the XRD pattern collected from both the vertical section (XZ-plane) and horizontal section (XY-plane) of the steel. It can be seen that both the planes exhibited insignificantly different patterns, where all the reflections were indexed to FCC austenite. No BCC ferrite was detected in the XRD pattern (Fig. 6), which is in agreement with previous studies on powder-bed fusion (PBF) fabricated 316L stainless steel [19, 25, 27]. However, some other studies have reported the BCC ferrite observation by XRD for the as-built 316L stainless steel parts produced by direct energy deposition (DED) techniques [22, 28].

EBSD technique was used to analyze the grain size and orientation of the samples. Typical EBSD orientation maps from both the vertical and horizontal sections of the as-built 316L stainless steel are illustrated in Fig. 7. From the vertical section—i.e. XZ-plane—(Fig. 7a), it is evident that the microstructure comprised mostly columnar grains with some equiaxed ones. The columnar grains, which are also observed in the directionally solidified microstructures [29], originated from epitaxial grain growth along heat flux direction (build direction). In the horizontal section—i.e. XY-plane—(Fig. 7b), the microstructure mainly consisted of equiaxed grains with some columnar ones. From the grain orientation point of view, no preferred crystallographic orientation existed within either vertical (Fig. 7a) or horizontal section (Fig. 7b), which can lead to approximately isotropic mechanical properties. The random orientation of the grains is attributed to the applied scan pattern, wherein the scan direction was rotated by 67° between the consecutive powder layers (Fig. 1).

A comparison between Figs. 5 and 7 will reveal the morphological relationship between the solidification cells and grain structure. In the vertical sections, where most cells were columnar (Fig. 5a), the grains were mainly columnar (Fig. 7a). Moreover, the horizontal section with majority of the equiaxed cells (Fig. 5a) was found to mostly comprise equiaxed grains (Fig. 7b). Thus, it can be concluded the morphology of the solidification cells in the as-built 316L stainless steel is highly dependent on the morphology of the grains containing them.

3.2 Micro-hardness analysis

Micro-hardness is considered as an important indicator of the mechanical property uniformity and isotropy in the additively manufactured parts. Figure 8 presents the micro-hardness profiles on both horizontal and vertical sections of the as-built 316L stainless steel, where each micro-hardness value is the average of five measurement results. Slight fluctuations of

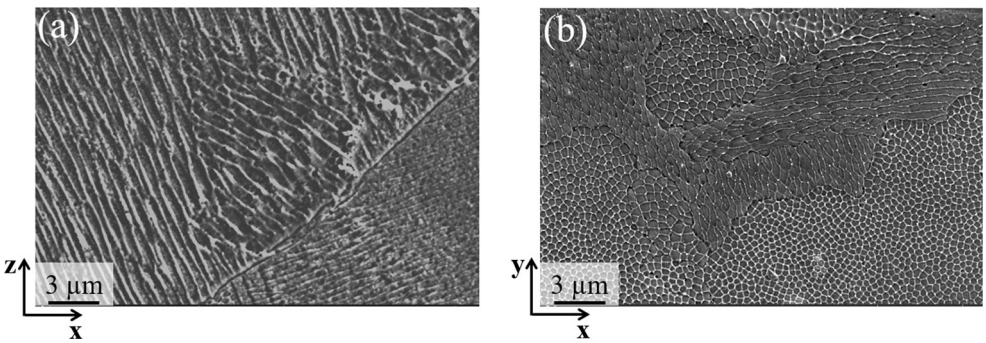

Fig. 5 Typical SEM micrographs from the vertical (**a**) and horizontal (**b**) sections of the DMLS-fabricated 316L stainless steel

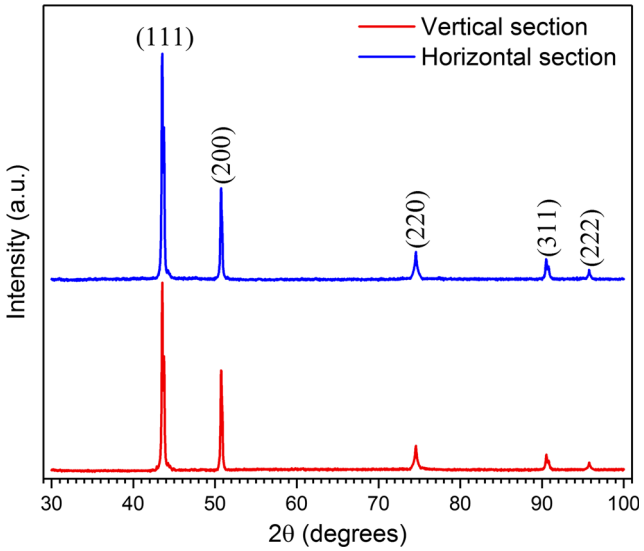

Fig. 6 XRD pattern of the as-built 316L stainless steel

micro-hardness values over five measurements—error bars in Fig. 8—are due to the presence of pores, unfused materials, balling, and micro-cracks. For both the sections, the micro-hardness values did not fluctuate significantly over long distances (20–22 mm), indicating the micro-hardness uniformity on each section. It seems that the overlapping of the adjacent scan tracks and successive deposited layers, which are often considered as metallurgically heterogonous locations, did not have any effects on the sample micro-hardness. The average micro-hardness value for the vertical section (XZ-plane) and horizontal section (XY-plane) was calculated to be 261 ± 8 and 269 ± 10 HV, respectively. The similarity of the average micro-hardness value for both the sections indicates the isotropy of the mechanical properties in the sample, which is a consequence of the random grain orientation observed in Fig. 7.

The average micro-hardness value of the as-built sample in this study was consistent with that of the 316L stainless steel fabricated by LENS (281 ± 25 HV) [22] and SLM (264 ± 8) [30]. Thus, it can be concluded that the AM technique type (PBF or DED) or process parameters (such as laser power, scan speed, hatch spacing, etc.) do not have a significant effect on the 316L stainless steel hardness. The average micro-hardness of the DMLS-fabricated 316L stainless steel in this contribution was approximately 25% higher than that of the as-cast one (210 HV) [26]. The extremely high solidification rate during AM processes result in finer grain structure than that obtained by conventional casting. Given that the material hardness is approximately proportional to its yield stress, the Hall-Petch relationship [31] can be employed to attribute the hardness enhancement of the AM parts to their smaller grain sizes. Nevertheless, it should be noted that this micro-harness enhancement compared to the as-cast steel will be associated with ductility degradation inherent to the ultrafine grains.

4 Conclusions

In this work, microstructural analysis and micro-hardness measurements were performed on different planes of the DMLS-fabricated disk-shaped 316L stainless steel. A fine cellular network was observed within the steel microstructure, where the cell boundaries were enriched in Mo. The XZ-plane (vertical section) microstructure comprised mostly columnar cells with some equiaxed ones, whereas the XY-plane (horizontal section) microstructure mainly consisted of equiaxed cells with some columnar ones. Correspondingly, morphology

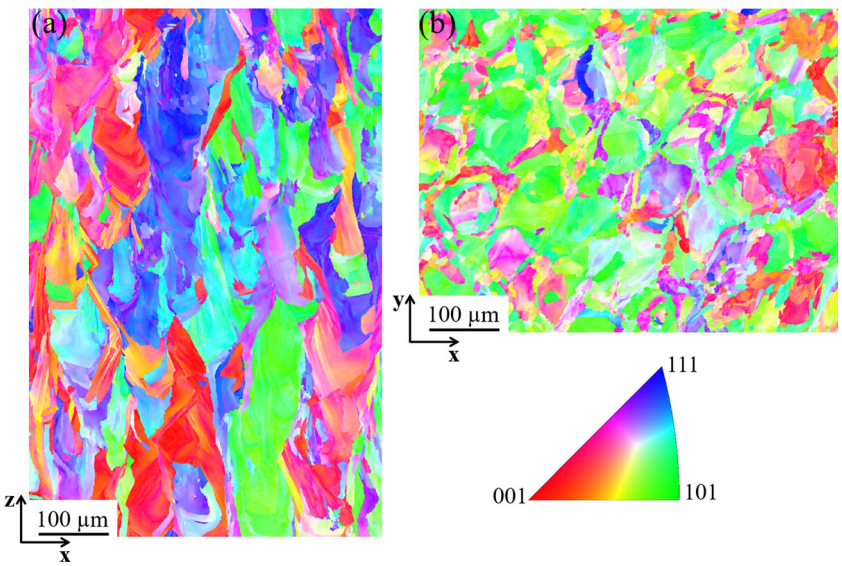

Fig. 7 Typical EBSD orientation maps of the as-fabricated 316L stainless steel. **a** Vertical section (XZ-plane). **b** Horizontal section (XY-plane)

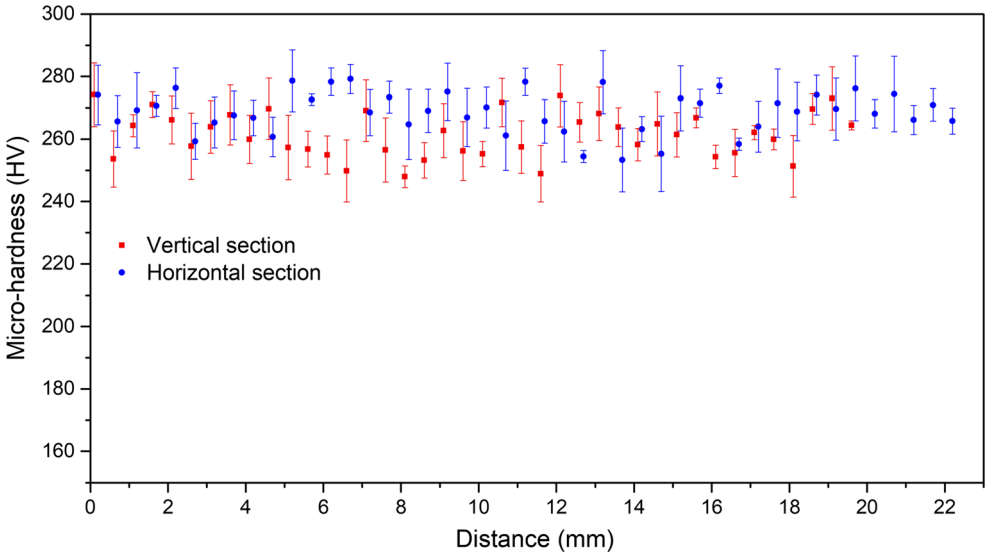

Fig. 8 Micro-hardness profile of the as-built 316L stainless steel

of most grains was found to change from columnar for the XZ-plane to equiaxed for the XY-plane. Moreover, both the planes exhibited a fully austenitic structure, as was revealed by X-ray diffraction (XRD) analysis. The average micro-hardness value of the XZ-plane was very similar to that of the XY-plane (less than 3% difference), which was attributed to the random grain orientation observed on both the planes. However, the average micro-hardness of the DMLS-fabricated 316L stainless steel in this study was approximately 25% greater than that of the as-cast one.

Acknowledgements This effort was performed through the National Center for Defense Manufacturing and Machining under the America Makes Program entitled "Parametric Design of Functional Support Structures for Metal Alloy Feedstocks (Project 4047)" and is based on research sponsored by Air Force Research Laboratory under agreement number FA8650-12-2-7230. The US Government is authorized to reproduce and distribute reprints for Governmental purposes notwithstanding any copyright notation thereon. The views and conclusions contained in this document are those of the authors and should not be interpreted as necessarily representing the official policies, either expressed or implied, of the Government.

Distribution authorized to US Government Agencies and America Makes Members; Critical Technology. Other request for this document shall be referred to AFRL/RXMS, Wright-Patterson Air Force Base, OH 45433–7750.

Compliance with ethical standards

Conflict of interest The authors declare that they have no conflict of interest.

References

1. Gu D, Meiners W, Wissenbach K, Poprawe R (2012) Laser additive manufacturing of metallic components: materials, processes and mechanisms. Int Mater Rev 57(3):133–164. https://doi.org/10.1179/1743280411Y.0000000014
2. Levy GN, Schindel R, Kruth J-P (2003) Rapid manufacturing and rapid tooling with layer manufacturing (LM) technologies, state of the art and future perspectives. CIRP Ann-Manuf Technol 52(2): 589–609. https://doi.org/10.1016/S0007-8506(07)60206-6
3. Berman B (2012) 3-D printing: the new industrial revolution. Business horizons 55(2):155–162. https://doi.org/10.1016/j.bushor.2011.11.003
4. Huang SH, Liu P, Mokasdar A, Hou L (2013) Additive manufacturing and its societal impact: a literature review. Int J Adv Manuf Technol:1–13
5. Atzeni E, Salmi A (2015) Study on unsupported overhangs of AlSi10Mg parts processed by direct metal laser sintering (DMLS). J Manuf Process 20:500–506. https://doi.org/10.1016/j.jmapro.2015.04.004
6. Aversa A, Lorusso M, Trevisan F, Ambrosio EP, Calignano F, Manfredi D, Biamino S, Fino P, Lombardi M, Pavese M (2017) Effect of process and post-process conditions on the mechanical properties of an A357 alloy produced via laser powder bed fusion. Metals 7(2):68. https://doi.org/10.3390/met7020068
7. Criales LE, Arısoy YM, Lane B, Moylan S, Donmez A, Özel T (2017) Laser powder bed fusion of nickel alloy 625: experimental investigations of effects of process parameters on melt pool size and shape with spatter analysis. Int J Mach Tools Manuf
8. Gribbin S, Bicknell J, Jorgensen L, Tsukrov I, Knezevic M (2016) Low cycle fatigue behavior of direct metal laser sintered Inconel alloy 718. Int J Fatigue 93:156–167. https://doi.org/10.1016/j.ijfatigue.2016.08.019
9. Kazantseva N, Krakhmalev P, Yadroitsev I, Fefelov A, Merkushev A, Ilyinikh M, Vinogradova N, Ezhov I, Kurennykh T (2017) Oxygen and nitrogen concentrations in the Ti-6Al-4V alloy manufactured by direct metal laser sintering (dmls) process. Mater Lett
10. AlMangour B, Yang J-M (2017) Understanding the deformation behavior of 17-4 precipitate hardenable stainless steel produced by direct metal laser sintering using micropillar compression and TEM. Int J Adv Manuf Technol 90(1–4):119–126. https://doi.org/10.1007/s00170-016-9367-9
11. Ghasri-Khouzani M, Peng H, Rogge R, Attardo R, Ostiguy P, Neidig J, Billo R, Hoelzle D, Shankar M (2017) Experimental measurement of residual stress and distortion in additively manufactured stainless steel components with various dimensions. Mater Sci Eng A 707:689-700. https://doi.org/10.1016/0956-7151(95)00110-H

12. Wang W, Kelly S (2016) A metallurgical evaluation of the powder-bed laser additive manufactured 4140 steel material. JOM 68(3): 869–875. https://doi.org/10.1007/s11837-015-1804-y
13. Gratton A (2012) Comparison of mechanical, metallurgical properties of 17-4ph stainless steel between direct metal laser sintering (DMLS) and traditional manufacturing methods. 2012 NCUR
14. Choi J-P, Shin G-H, Brochu M, Kim Y-J, Yang S-S, Kim K-T, Yang D-Y, Lee C-W, Yu J-H (2016) Densification behavior of 316L stainless steel parts fabricated by selective laser melting by variation in laser energy density. Mater Trans 57(11):1952–1959. https://doi.org/10.2320/matertrans.M2016284
15. Delgado J, Ciurana J, Serenó L (2011) Comparison of forming manufacturing processes and selective laser melting technology based on the mechanical properties of products: in this work, the superior property of the selective laser melting technology is presented by comparing four real parts manufactured using forming processes and selective laser melting technology and analysed for tension, compression and flexural. Virtual Phys Prototyp 6(3):167–178
16. Yu J, Rombouts M, Maes G (2013) Cracking behavior and mechanical properties of austenitic stainless steel parts produced by laser metal deposition. Mater Des 45:228–235. https://doi.org/10.1016/j.matdes.2012.08.078
17. de Lima MSF, Sankaré S (2014) Microstructure and mechanical behavior of laser additive manufactured AISI 316 stainless steel stringers. Mater Des 55:526–532. https://doi.org/10.1016/j.matdes.2013.10.016
18. Mertens A, Reginster S, Contrepois Q, Dormal T, Lemaire O, Lecomte-Beckers J (2014) Microstructures and mechanical properties of stainless steel AISI 316L processed by selective laser melting. Mater Sci Forum 786:898–903
19. Saeidi K, Gao X, Zhong Y, Shen ZJ (2015) Hardened austenite steel with columnar sub-grain structure formed by laser melting. Mater Sci Eng A 625:221–229. https://doi.org/10.1016/j.msea.2014.12.018
20. Wang D, Song C, Yang Y, Bai Y (2016) Investigation of crystal growth mechanism during selective laser melting and mechanical property characterization of 316L stainless steel parts. Mater Des 100:291–299. https://doi.org/10.1016/j.matdes.2016.03.111
21. Zhang K, Wang S, Liu W, Shang X (2014) Characterization of stainless steel parts by laser metal deposition shaping. Mater Des 55:104–119. https://doi.org/10.1016/j.matdes.2013.09.006
22. Zietala M, Durejko T, Polanski M, Kunce I, Plocinski T, Zielinski W, Lazinska M, Stepniowski W, Czujko T, Kurzydlowski KJ (2016) The microstructure, mechanical properties and corrosion resistance of 316 L stainless steel fabricated using laser engineered net shaping. Materials science and engineering a—structural materials properties microstructure and processing 677 (EPFL-ARTICLE-225036):1-10
23. Manvatkar V, Gokhale A, Reddy GJ, Venkataramana A, De A (2011) Estimation of melt pool dimensions, thermal cycle, and hardness distribution in the laser-engineered net shaping process of austenitic stainless steel. Metall Mater Trans A 42(13):4080–4087. https://doi.org/10.1007/s11661-011-0787-8
24. Li R, Shi Y, Wang Z, Wang L, Liu J, Jiang W (2010) Densification behavior of gas and water atomized 316L stainless steel powder during selective laser melting. Appl Surf Sci 256(13):4350–4356. https://doi.org/10.1016/j.apsusc.2010.02.030
25. Trelewicz JR, Halada GP, Donaldson OK, Manogharan G (2016) Microstructure and corrosion resistance of laser additively manufactured 316L stainless steel. JOM 68(3):850–859. https://doi.org/10.1007/s11837-016-1822-4
26. Mataya MC, Nilsson ER, Brown EL, Krauss G (2003) Hot working and recrystallization of as-cast 316L. Metall Mater Trans A 34(8): 1683–1703. https://doi.org/10.1007/s11661-003-0313-8
27. Zhong Y, Liu L, Wikman S, Cui D, Shen Z (2016) Intragranular cellular segregation network structure strengthening 316L stainless steel prepared by selective laser melting. J Nucl Mater 470:170–178. https://doi.org/10.1016/j.jnucmat.2015.12.034
28. Guo P, Zou B, Huang C, Gao H (2017) Study on microstructure, mechanical properties and machinability of efficiently additive manufactured AISI 316L stainless steel by high-power direct laser deposition. J Mater Process Technol 240:12–22. https://doi.org/10.1016/j.jmatprotec.2016.09.005
29. Ferrandini P, Rios C, Dutra A, Jaime M, Mei P, Caram R (2006) Solute segregation and microstructure of directionally solidified austenitic stainless steel. Mater Sci Eng A 435:139–144
30. Yang Y, Lu J-b, Luo Z-Y, Wang D (2012) Accuracy and density optimization in directly fabricating customized orthodontic production by selective laser melting. Rapid Prototyp J 18(6):482–489. https://doi.org/10.1108/13552541211272027
31. Kashyap B, Tangri K (1995) On the Hall-Petch relationship and substructural evolution in type 316L stainless steel. Acta Metall Mater 43(11):3971–3981. https://doi.org/10.1016/0956-7151(95)00110-H